J. Fluid Mech. (2023), *vol*. 971, A6, doi:10.1017/jfm.2023.594

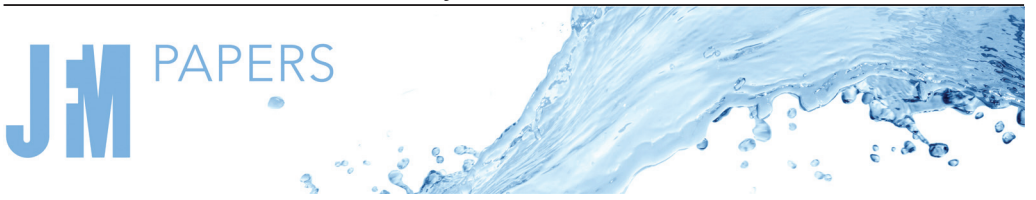

Inviscid evolution of a uniform vortex dipole in a strain field

JiaCheng Hu[1] **and Sean D. Peterson**[1],†

[1]Department of Mechanical and Mechatronics Engineering, University of Waterloo, Waterloo ON N2L 3G1, Canada

(Received 13 October 2022; revised 24 April 2023; accepted 8 July 2023)

Competing models employing anti-parallel vortex collision in search of a finite-time singularity of Euler's equation have arisen recently. Both the vortex sheet model proposed by Brenner *et al.* (*Phys. Rev. Fluids*, vol. 1, 2016, 084503) and the 'tent' model proposed by Moffatt & Kimura (*J. Fluid Mech.*, vol. 861, 2019, pp. 930–967) consider a vortex monopole exposed to a strain flow to model the evolution of interacting anti-parallel vortices, a fundamental element in the turbulent cascade. Herein we employ contour dynamics to explore the inviscid evolution of a vortex dipole subjected to an external strain flow with and without axial stretching. We find that for any strain-to-vorticity ratio $\mathcal{E}$, the constituent vortices compress indefinitely, with weaker strain flows causing flattening to occur more slowly. At low $\mathcal{E}$, the vortex dipole forms the well-documented head–tail structure, whereas increasing $\mathcal{E}$ results in the dipole compressing into a pair of vortex sheets with no appreciable head structure. Axial stretching effectively lowers $\mathcal{E}$ dynamically throughout the evolution, thus delaying the transition from the head–tail regime to the vortex sheet regime to higher strain-to-vorticity ratios. Findings from this study offer a bridge between the two cascade models, with the particular mechanism arising depending on $\mathcal{E}$. It also suggests limits for the 'tent' model for a finite-time singularity, wherein the curvature-induced strain flow must be very weak in comparison with the vorticity density-driven mutual attraction such that the convective time scale of the evolution exceeds the core flattening time scale.

Key words: vortex dynamics, turbulence theory, contour dynamics

1. Introduction

The vortex monopole/column is a fundamental element used to explore the dynamics of coherent vortices in turbulence. Moore & Saffman (1971) first considered an inviscid

† Email address for correspondence: peterson@uwaterloo.ca

column vortex subject to a planar irrotational strain field where the principal strain axes are perpendicular to the vortex axis. They found that weak strain-to-vorticity ratios result in an elliptical vortex that nutates around its centre. In subsequent numerical simulations, Kida (1981) noted that above a certain strain-to-vorticity threshold, the solution bifurcates, and the vortex flattens into a sheet. Neu (1984) investigated analytically the influence of axial stretching on a strained vortex monopole, and found that stretching delays the critical bifurcation point to a higher strain-to-vorticity ratio. Subsequently, Moffatt, Kida & Ohkitani (1994) generalized the motion of a vortex column in a uniform non-axisymmetric irrotational strain field using large Reynolds number asymptotic theory. They showed that strained vortices undergoing axial stretching could survive for a long time in a viscous flow, consistent with the observed persistence of vortex filaments in turbulent flows.

While analysis of a single vortex column in a strain field provides compelling descriptions of vortex dynamics in turbulent flows, recent surveys of turbulence have shown the tendency of anti-parallel vortex pairs to form (Goto, Saito & Kawahara 2017; Motoori & Goto 2019) (see also the excellent review article by Yao & Hussain 2021). McKeown *et al.* (2018) observed experimentally an iterative process of colliding anti-parallel vortices, wherein the vortices first flatten into thin vortex sheets, then roll up into smaller anti-parallel vortices that subsequently collide and then flatten into another set of smaller vortex sheets, and so on. An elemental analysis of this iterative flattening process using the vortex monopole model by Brenner, Hormoz & Pumir (2016), which assumed that the strain field sourced from pairing vortices is sufficient to flatten a vortex core, suggested the possibility of a finite-time singularity for Euler's equation. However, a subsequent theoretical analysis of anti-parallel vortex collision by Moffatt & Kimura (2019*a*) found that mutually induced strain from pairing vortices is insufficient to flatten their cores. Their analysis, based on the vortex monopole model with the imposed strain field extracted from anti-parallel vortex pairs using the Biot–Savart law, shows that if the vortices are sufficiently small (low strain-to-vorticity ratio), then the cores maintain their compactness. As such, they concluded that a finite-time singularity could not be achieved by the iterative flattening process. Rather, they proposed that an inviscid finite-time singularity can be achieved via the so-called 'tent' process, where vortex motion between colliding vortices results in a singularity at the apex of the 'tent'. Numerical simulations by Yao & Hussain (2020*b*), however, disputed their claim of vortex compactness, as they found core flattening during an analogous collision of anti-parallel vortices with the core size limit suggested by Moffatt & Kimura (2019*a*).

It is important to note that the Biot–Savart singularity of colliding anti-parallel vortex pairs was considered decades ago by Siggia & Pumir (1985), and then via simulations of Euler's equations by Pumir & Siggia (1990). They pointed out that the flattening of vortex cores is one of the primary factors preventing singularities in Euler's equations, despite encouraging Biot–Savart analyses. A potential culprit contributing to this disagreement between theoretical predictions and experimental and numerical observations of colliding anti-parallel vortex pairs may lie in the applicability of a strained vortex monopole as a model of the dynamics.

The evolution of a strained vortex dipole is a relatively unexplored topic. Formation of a head–tail structure for a strained dipole was first reported by Buntine & Pullin (1989). Subsequently, Kida, Takaoka & Hussain (1991*b*) improved the initial conditions of the simulations by employing a Lamb dipole and tested a small range of strain-to-vorticity ratios. They observed that the relative sizes of the head and tail depend strongly on this ratio. They further demonstrated via perturbation analysis that the interaction with the background strain flow introduced a symmetry breaking term, which is the cause

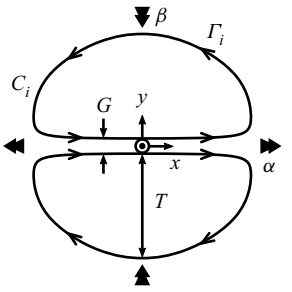

Figure 1. Schematic of a vortex dipole in a strain field, with relevant variables indicated.

of head–tail formation. Trieling, Van Wesenbeeck & Van Heijst (1998) validated the simulation results experimentally. These studies were limited to low Reynolds numbers, where the dynamics was dominated by viscous effects, which are also known to produce a head–tail structure (Kida, Takaoka & Hussain 1991*a*; Delbende & Rossi 2009). As such, our present understanding of the role of strain flow on vortex dipole dynamics is confounded by viscous effects, making it difficult to extend these findings to high Reynolds number turbulent and inviscid flows. Furthermore, only planar strain was considered in these studies, and the range of strain-to-vorticity ratios explored was limited.

Herein, we examine the behaviour of a vortex dipole in an inviscid converging strain flow using contour dynamics. Specifically, we consider the impacts of strain-to-vorticity ratio and axial stretching on vortex dipole conformation evolution in an effort to explain the apparent disagreement between theoretical predictions (Moffatt & Kimura 2019*a*) and numerical and experimental observations (McKeown *et al.* 2018; Yao & Hussain 2020*b*) of colliding anti-parallel vortex pairs.

The paper is organized as follows. Section 2 outlines the problem formulation and numerical set-up. Section 3 explores the evolution of vortex dipoles under planar strain, and § 4 considers the effect of axial stretching on dipole evolution. Section 5 discusses implications of the present study on the search for a finite-time singularity of Euler's equation and the turbulent cascade, and § 6 concludes the work. A brief review of the motion of a strained vortex monopole is presented in Appendix A, and validation of our numerical contour dynamics scheme is provided in Appendix B.

2. Problem statement

We consider a vortex dipole in an unbounded ideal fluid. A Cartesian coordinate system $\boldsymbol{x} = (x, y, z)$ is defined such that the x-axis is aligned with the self-induction direction of the vortex dipole, and the z-axis is parallel to the vortex lines, as shown in figure 1. The vortex dipole consists of two uniform vorticity patches bounded by contours C_i, where the subscript $i = 1, 2$ designates the top (positive y) and bottom (negative y) patches, respectively. The vortex patches have opposing circulations $\Gamma_i = \pm A_i(t)\,\Omega_i(t)$ (top patch positive), where $\Omega_i(t)$ and $A_i(t)$ are the uniform vorticity patch magnitude and area, respectively. The initial uniform vorticity magnitude of each patch is given by $\Omega_0 = \Omega_i(t = 0)$.

2.1. *Strain field*

A three-dimensional irrotational uniform strain flow $\boldsymbol{u}_s(\boldsymbol{x}) = (\alpha x, \beta y, \gamma z)$ is imposed, where α, β and γ are the strain rates along each coordinate direction. This strain flow

	α/Ω_0	β/Ω_0	γ/Ω_0
Planar	$\mathcal{E}$	$-\mathcal{E}$	0
Low	$\mathcal{E}/2$	$-\mathcal{E}$	$\mathcal{E}/2$
High	0	$-\mathcal{E}$	$\mathcal{E}$
Axisymmetrical	$-\mathcal{E}$	$-\mathcal{E}$	$2\mathcal{E}$

Table 1. Irrotational strain flows considered, where Ω_0 is the initial vortex patch vorticity magnitude, and $\mathcal{E}$ is the strain-to-vorticity ratio.

has its principal axes aligned with the vortex dipole and continuity constraints such that $\alpha + \beta + \gamma = 0$. We note that if the strain flow was not aligned with the dipole principal axes, then a rotational component on the dipole would arise, which is not of concern in the present study, and is hence not considered herein. We restrict $\beta < 0$ such that the y-component of the strain flow acts to squeeze the two vortices together. For $\beta > 0$, the dipole splits into two monopoles that then evolve separately with minimal coupled dynamics (Trieling *et al.* 1998).

Four types of strain fields are considered, as listed in table 1, where the initial strain-to-vorticity ratio is denoted $\mathcal{E}$. The first type is a planar strain field with equal but opposite strain rates in the x–y plane, and no axial stretching (along the z-axis). This is analogous to the strain fields employed in previous studies (Buntine & Pullin 1989; Kida *et al.* 1991*a*; Trieling *et al.* 1998). The second type of strain field is a low axial strain field. This is achieved by decreasing the expansion rate in the x-direction by half to compensate for the increase in z-axis stretching. The third type is a high axial stretching strain field with equal magnitudes of compression and stretching along the y- and z-directions, respectively. Note that the 'low' and 'high' axial strain rates are meant only as relative descriptors herein as we examine the effect of axial stretching; they do not represent any limiting cases. Finally, the limiting case of axisymmetrical stretching is considered.

For each strain type, the strain-to-vorticity ratio is varied systematically in $0 \leq \mathcal{E} \leq 1$. The ratio is bounded from above by unity, based upon pilot studies that found no significant change in the behaviour for $\mathcal{E} > 1$ as the motion is dominated by the external strain flow.

2.2. *Contour dynamics*

The induced velocity by the uniform vortex patches at any point $\boldsymbol{u}_\omega(\boldsymbol{x})$ is computed from

$$\boldsymbol{u}_\omega(\boldsymbol{x}) = -\frac{1}{2\pi}\sum_{i=1}^{2}\Omega_i(t)\int_{C_i}\ln|\boldsymbol{x}-\boldsymbol{x}'|\,\mathrm{d}\boldsymbol{l}', \tag{2.1}$$

where $\mathrm{d}\boldsymbol{l}'$ is the infinitesimal boundary segment at $\boldsymbol{x}'$ (Zabusky, Hughes & Roberts 1979), and t is time. Though contour dynamics is a purely two-dimensional method, the effect of axial stretching can be captured analytically as

$$\Omega(t) = \Omega_0\exp(\gamma t) \tag{2.2}$$

(Neu 1984; Jacobs & Pullin 1985). That is, axial stretching acts essentially to dynamically decrease the strain-to-vorticity ratio $\mathcal{E}$ throughout the interaction when $\gamma > 0$.

2.3. *Numerical scheme*

The total velocity at any point is

$$\boldsymbol{u}(\boldsymbol{x}) = \boldsymbol{u}_{\omega}(\boldsymbol{x}) + \boldsymbol{u}_{s}(\boldsymbol{x}), \tag{2.3}$$

which is a combination of both the background strain flow $\boldsymbol{u}_s(\boldsymbol{x})$ and the vortex induced flow $\boldsymbol{u}_\omega(\boldsymbol{x})$. To compute the evolution of the vortex motion, we discretize the vortex contours into a collection of linear segments. The integral in (2.1) is evaluated in closed form along each linear segment, then summed, along with the strain flow, to compute the total induced velocity at each of the endpoints of the line segments. The line segments are then advected in time using an adaptive eighth-order explicit Runge–Kutta method. For all simulations in this study, the contours are discretized into 1024 segments. Note that 1024 segments are employed based upon a convergence study, and we found no observable difference in the quantities of interest when comparing 1024 and 2048 segment solutions. Dynamic re-discretization of line segments is performed after every time step for two reasons: because discretization points become unevenly distributed and clustered after some time, which significantly corrupts the accuracy; and to ensure that curvatures are properly resolved. We note that we redistribute only the discretization points, but maintain a fixed number of segments to ensure computational efficiency. A symmetry condition between the two halves of the dipole is implemented to improve computational efficiency, as past studies of strained vortex dipoles have found them to maintain their top–bottom symmetry (Buntine & Pullin 1989; Kida *et al.* 1991*a*; Trieling *et al.* 1998). Numerical simulations were run up to non-dimensional times $t\,|\beta| = 10$.

The numerical scheme is validated in two ways: by checking that circulation is conserved; and via comparison with classical examples in contour dynamics. Regarding circulation, since the vortex patches have uniformly distributed vorticity, conservation of circulation is equivalent to conservation of area, such that (2.2) becomes $A(t) = A(0)\exp(-\gamma t)$. The deviation in the vortex patch area for all results presented herein is less than 0.1 %, indicating that throughout the patch evolution, the number of elements and their re-discretization are sufficient. In addition, several classical examples of contour dynamics were solved using the present numerical scheme, including a strained vortex monopole (Kida 1981; Neu 1984), the Kirchhoff elliptic vortex (Dritschel 1986; Mitchell & Rossi 2008), and coalescence of two equal same-signed vortices (Zabusky *et al.* 1979; Jacobs & Pullin 1985). Samples of the solutions to these classical problems are presented in Appendix B, which agree very well with solutions documented in the literature.

2.4. *Initial conditions*

Special consideration for the initial condition is required since circular vortex dipole cores produce unrealistic deformations (Kida *et al.* 1991*a*). Rather, an inviscid strain-free vortex dipole (the limiting case of $\mathcal{E} = 0$, also known as a Lamb–Chaplygin dipole; Meleshko & van Heijst 1994), which travels steadily with no self-induced deformation and maintains its twofold symmetry (front–back and top–bottom), is used herein. To establish such an initial condition for our simulations, we employ the method developed by Pierrehumbert (1980). In short, the method relies on the fact that a steady vortex dipole has a constant stream function value along its bounding contour. Hence the shape of a steady uniform vorticity vortex dipole can be found by adjusting its contour until the streamfunction value becomes constant at the vortex boundary using an iterative optimization algorithm.

The shape of the vortex core can be controlled through the gap ratio $G/(G + 2T)$, where G is the minimum gap length in the y-direction, and T is the maximum thickness of

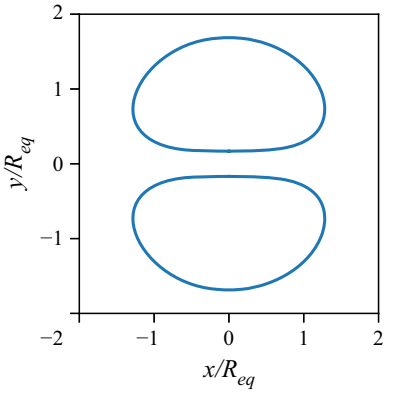

Figure 2. Initial condition of a vortex dipole with a gap ratio $G/(G+2T) = 0.1$.

the vortex patch in the y-direction (see figure 1). A gap ratio 0.1 is employed herein, which produces the vortex dipole shown in figure 2. Note that $R_{eq} = \sqrt{A(t=0)/\pi}$ is the equivalent radius of the vortex core, which is employed as the characteristic length scale in this study.

A non-zero gap ratio is employed for two reasons. First, it is unreasonable to assume that only axial touching vortex pairs exist in turbulent flows, and we wish to examine the nonlinear collision dynamics driven by an external/curvature-induced strain field. Second, Moffatt & Kimura (2019*b*) have shown that colliding vortices (their 'tent' model) reach an asymptotic value $y_c/R_{eq} = 0.7788$, where y_c is the core centroid position, at the time of the Biot–Savart singularity. Our initial condition has a value $y_c/R_{eq} = 0.8736$, which permits us to evaluate the vortex core behaviour prior to the reported singular value under the influence of curvature-induced strain.

3. Planar strain field

Three strain-to-vorticity ratios, $\mathcal{E} = 0.05$, 0.2 and 0.4, are considered to highlight vortex dipole behaviours under the applied plane strain field introduced in table 1. Evolution of the dipole contours for $\mathcal{E} = 0.05$ is shown in figure 3, which illustrates a typical formation of the head–tail structure of a strained vortex dipole (Kida & Takaoka 1994; Hussain & Duraisamy 2011). In figure 3(*b*), the dipole halves are being squeezed together under the converging strain flow, which decreases the gap between the dipole halves and deforms their shape. As time continues, the classical head–tail structure arises, with the cores initially beginning to touch (figure 3*c*) followed by progressive elongation and thinning of the tail (figures 3*d–f*). As the tail grows, the leading dipole shape initially resembles a strain-free axially touching vortex dipole (figure 3*d*) (Pierrehumbert 1980; Saffman & Tanveer 1982), which continues to shrink as vorticity is ejected into the tail (figures 3*e*,*f*).

The dipole behaviour begins to change with an increase in the strain-to-vorticity ratio to $\mathcal{E} = 0.2$, as shown in figure 4. The vortex cores are far more stretched out in the x-direction, to the point where the leading region of the dipole exhibits no appreciable bulging (figures 4*c*,*d*). However, the profile of the vortex patches is still thickest near the leading edges, which then taper off into a tail (figures 4*d*,*e*). At $t\,|\beta| = 1.5$ (figure 4*f*), the bulges near the leading edge finally emerge, indicating that there is still a head–tail structure, but with much of the circulation embedded in the tail.

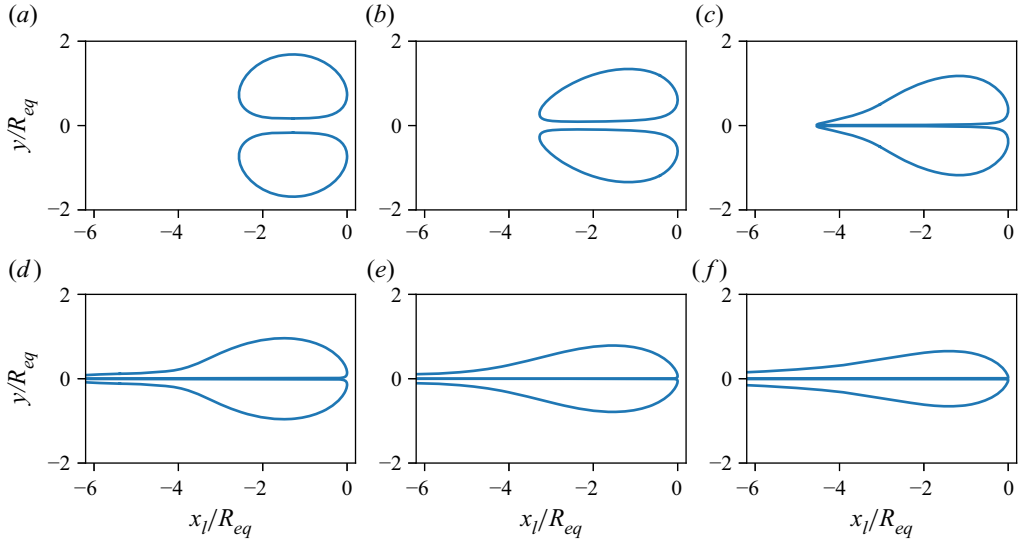

Figure 3. Contour evolution of a vortex dipole in a planar strain field with $\mathcal{E} = 0.05$. Snapshots from $t\,|\beta| = 0$ to 1.5 at intervals of 0.3 are shown from (*a*) to (*f*). The contours at each time step are aligned at their leading edge x_l for ease of comparison.

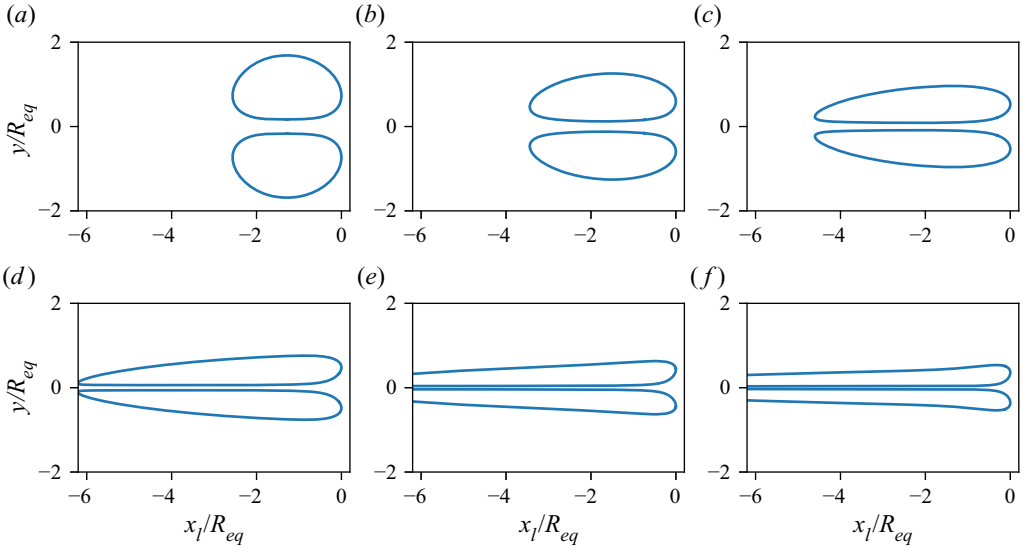

Figure 4. Contour evolution of a vortex dipole in a planar strain field with $\mathcal{E} = 0.2$. Snapshots from $t\,|\beta| = 0$ to 1.5 at intervals of 0.3 are shown from (*a*) to (*f*). The contours at each time step are aligned at their leading edge x_l for ease of comparison.

With a sufficiently large strain-to-vorticity ratio, the dipole is flattened completely into vortex sheets, as shown in figure 5 for $\mathcal{E} = 0.4$. During the early stages of the evolution, the vortex patches are mostly left–right symmetrical, as seen in figures 5(*a–c*), which is an early indication of a change in regime. As time continues (figures 5*d–f*), the patches become completely flattened into sheets. At $t\,|\beta| = 1.5$ (figure 5*f*), the vortex patches have a near-uniform thickness along their length, with the leading edges forming a

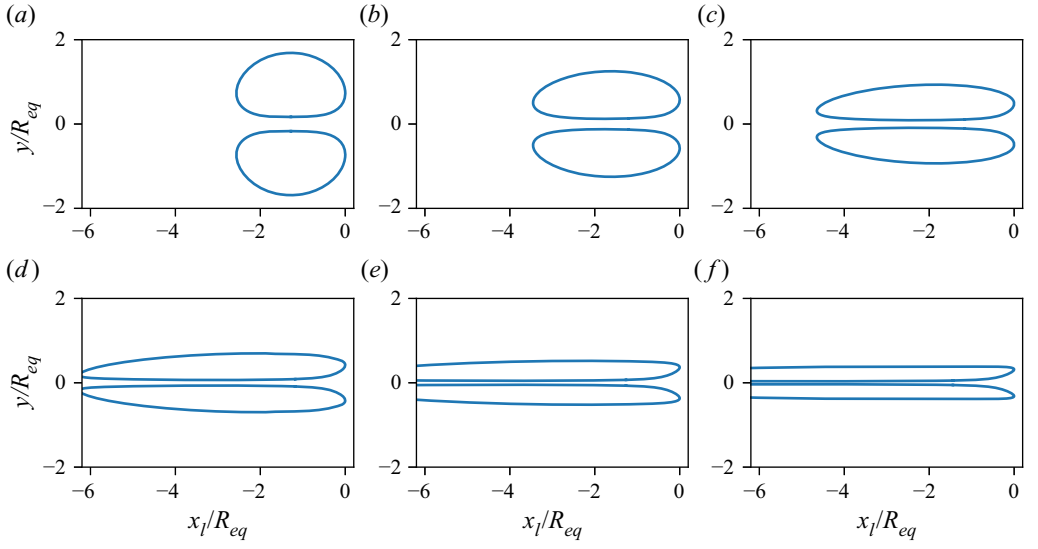

Figure 5. Contour evolution of a vortex dipole in a planar strain field with $\mathcal{E} = 0.4$. Snapshots from $t\,|\beta| = 0$ to 1.5 at intervals of 0.3 are shown from (*a*) to (*f*). The contours at each time step are aligned at their leading edge x_l for ease of comparison.

diffuser-like shape. The pairing of the vortex sheets induces a planar jet along the x-axis that is ejected into the ambient environment.

3.1. *Dipole thickness*

The compactness of monopoles can be quantified easily via the ratio between the principal axes of their elliptical form (Kida 1981; Neu 1984). However, there is no predetermined form for dipole deformation, hence a new descriptor is needed to measure the 'compactness' of the deformed vortex dipole patches. Observing that the deformations are always aligned with the axes of the strain field (see, for example, figure 4), we employ the maximum thickness $T(t)$ of the vortex patch (see figure 1) as a proxy measure of the compactness of the dipole patches, as a decrease in thickness corresponds to flattening of the vortex patches.

Temporal evolution of the maximum thickness $T(t)$ for all considered planar strain field cases is illustrated in figure 6(*a*), normalized by the initial thickness $T(0)$. Overall, there is a decreasing trend regardless of the strength of the strain field, with all cases ultimately approaching zero thickness asymptotically. That is, unlike the vortex monopole, the cores of the vortex dipole do not arrive at a 'final compactness', even for the head–tail regime. This highlights a limitation of the analogy with monopole compactness. Rather than comparing the aspect ratio, dipole 'compactness', represented here as dipole thickness, has meaning only in a relative sense at a given time point. As discussed in Appendix A, a vortex monopole combats the strain field via self-induced rotation that causes the principal axes to flatten and contract in a periodic manner. For a vortex dipole, however, the pairing essentially creates a slip wall that prevents the principal axes of each component vortex patch from rotating. As such, the axes of deformation are always aligned with the strain field, thus the patches flatten continually and increasingly.

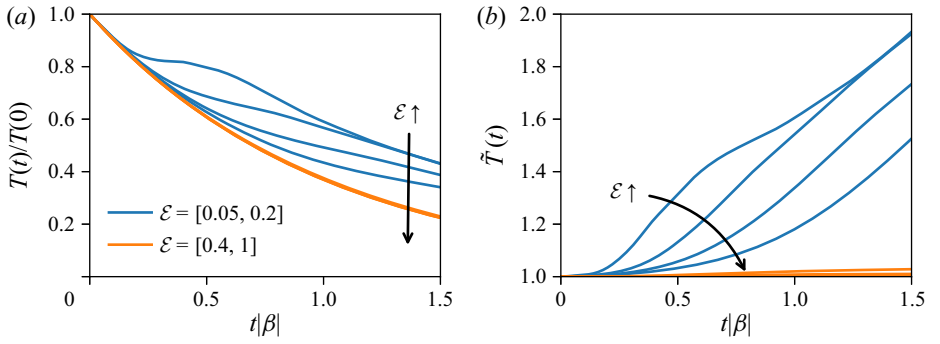

Figure 6. Temporal evolution of vortex dipole patch (*a*) thickness $T(t)$, and (*b*) normalized thickness $\tilde{T}(t)$, for the planar strain field cases. The head–tail regimes between $\mathcal{E} = 0.05, 0.1, 0.15, 0.2$ are shown in blue, while the plane jet regimes between $\mathcal{E} = 0.4, 0.6, 0.8, 1.0$ are shown in orange.

To isolate the effect of vorticity, we consider normalized thickness $\tilde{T}(t)$, defined as

$$\tilde{T}(t) = \frac{T(t)}{T(0)\exp(\beta t)}. \tag{3.1}$$

The denominator represents the thickness evolution of a simple material contour subjected purely to the strain flow. A value of normalized thickness greater than 1 indicates that vorticity decelerates the strain-field-induced flattening. Normalized thickness presented in figure 6(*b*) clearly shows two trends. First, for cases $\mathcal{E} = 0.05, 0.1, 0.15, 0.2$, there is a continuous and rapid growth of the normalized thickness, indicating that vorticity provides some 'resistance' to the strain flow as it works to flatten the dipole. Interestingly, these cases correspond to the head–tail regime. That is, the 'resistance' arises from the same left–right flow field asymmetry that creates the head–tail structure Kida *et al.* (1991*a*), a mechanism that is absent from a vortex monopole.

For cases $\mathcal{E} = 0.4, 0.6, 0.8, 1.0$, the normalized thickness remains near unity for the entirety of the simulation (up to $t|\beta| = 10$). These cases correspond to the planar jet regime, where the head–tail formation is arrested by the strain flow, preventing any vorticity from collecting at the leading edges. Vorticity for these cases does not decelerate appreciably the strain-induced flattening. The rate of flattening for the planar jet regime is much faster than for monopoles under the same strain flow since monopole self-rotation changes the relative angle of the principal axes with respect to the strain field; see Appendix A.

3.2. *Mutual attraction*

Contrasting the cases of $\mathcal{E} = 0.05$ and $\mathcal{E} = 0.4$ in figures 3 and 5 suggests an interesting and counterintuitive aspect of dipoles in a planar strain field, namely that a weak strain flow forces the two comprising patches together at a faster rate than does a high strain field. For the head–tail regime in figures 3(*a–c*), the gap between the patches tends to decrease from head to tail, whereas the minimum for the gap in the planar jet regime in figure 5(*b*) is at approximately the middle of the dipole.

To quantify the patch separation distance, we introduce the gap length $G(t)$, defined as the minimum distance between the patches (figure 1), and present it in figure 7(*a*) for all cases. The cases with $\mathcal{E} \leq 0.2$ exhibit rapid decreases in gap spacing, with $\mathcal{E} = 0.05$ showing the most rapid approach of the vortex patches towards one another. On the other

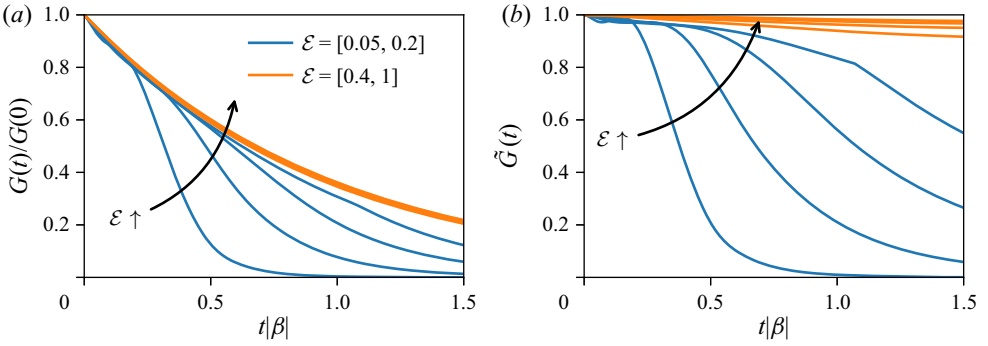

Figure 7. Temporal evolution of (*a*) gap length $G(t)$ and (*b*) normalized gap length $\tilde{G}(t)$ between vortex patches. The head–tail regimes between $\mathcal{E} = 0.05, 0.1, 0.15, 0.2$ are shown in blue, while the plane jet regimes between $\mathcal{E} = 0.4, 0.6, 0.8, 1.0$ are shown in orange.

hand, while cases with $\mathcal{E} \geq 0.4$ still show a decrease in the gap between the patches, the rate of approach is much slower, and there is a marginal influence of strain-to-vorticity ratio.

The influence of vorticity can be isolated from that of the strain flow, which also squeezes the patches together, by normalizing the gap length as $\tilde{G} = G(t)/\exp(-t\,|\beta|)$; see figure 7(*b*). As with normalized thickness, the denominator originates from the analytical solution of a simple material contour without vorticity, where the gap reduces exponentially under the strain flow. Thus a line with a zero slope indicates that the gaps are closed under the strain flow exclusively. Any deviation from a horizontal line indicates that other effects are at play. The time series in figure 7(*b*) for $\mathcal{E} \leq 0.2$ deviates noticeably from $\tilde{G} = 1$, indicating that gap closure is strongly aided by vorticity. For cases with $\mathcal{E} \geq 0.4$, the curves deviate only slightly from unity, demonstrating that the patches are primarily closed under the influence of the strain flow.

The mechanism by which vorticity aids in driving the patches together warrants additional consideration. Though it may be enticing to attribute this to the flow induced by the dipole head on its tail in figure 3, vorticity-driven closing is still prominent in cases without a prominent leading dipole (e.g. the $\mathcal{E} = 0.15$ case in figure 4). Furthermore, the gap in figure 4 decreases relatively uniformly in space, without any localized throat area between the patches that would hint at the role of the leading dipole. That said, the intuitive leading dipole explanation can be generalized to provide insight into the mechanism by which vorticity drives the patches together. As illustrated schematically in figure 8, the local thickness of a vortex patch is proportional to the circulation at that location. The thickness of the patch generally increases from 'tail' (left) to 'head' (right), resulting in an increasing gradient of circulation along the deformed dipole. This circulation differential produces a net inward flow (blue arrows in figure 8) that drives a self-induced motion of each patch towards the centreline, similar to that of a potential flow vortex sheet with a circulation strength gradient. Therefore, the observed enhanced mutual attraction is a direct consequence of asymmetrical deformation inherent to a vortex dipole in a compressive strain field (Kida *et al.* 1991*a*).

4. Axial stretching

In this section, we present the results of strain flow with axial stretching (see table 1). As discussed in § 2, axial stretching amplifies the vorticity relative to the strain field as

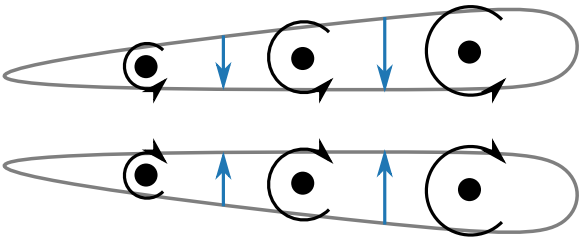

Figure 8. Schematic illustrating the mechanism by which vorticity distribution drives the vortex patches towards one another. The size of the black 'vortices' indicates local circulation; blue arrows show the magnitude and direction of induced inward flow.

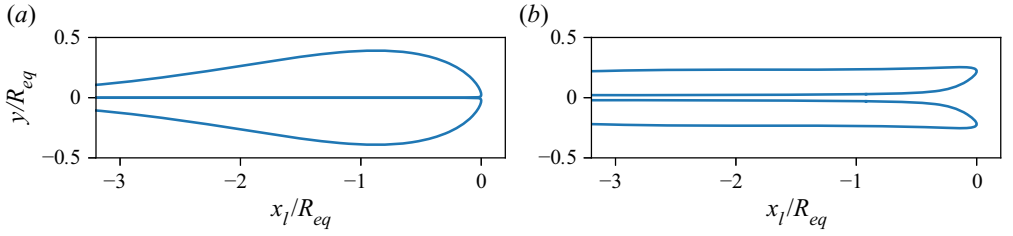

Figure 9. Contour snapshots of (*a*) $\mathcal{E} = 0.1$ and (*b*) $\mathcal{E} = 0.8$ at $t\,|\beta| = 2$ for the low axial stretching case.

time progresses, effectively lowering $\mathcal{E}$ dynamically. Based upon the analysis in § 3, the transition from the head–tail regime to the planar jet regime is expected to occur at higher values of strain-to-vorticity ratio $\mathcal{E}$ under the action of axial stretching. Indeed, snapshots of vortex contours shown in figure 9 for the head–tail and planar jet regimes are similar in structure to the planar strain cases presented in § 3 for low axial stretch stretching cases (see table 1 for definition).

The normalized thickness and gap presented in figure 10 are qualitatively similar to the planar strain results, albeit with the aforementioned delay of regime transition to higher $\mathcal{E}$. Normalized thickness in figure 10(*a*) shows that for a given $\mathcal{E}$, there is less flattening than in the planar strain case. For $\mathcal{E} = 0.6$ and 0.8, the rate at which thickness decreases begins to reduce after $t\,|\beta| > 1.5$ (normalized thickness begins to increase) because the leading edge of the vortex sheet begins to re-spiral into a vortex core under the aid of axial stretching. As for the gap length in figure 10(*b*), the range of mutual attraction expands with increasing vorticity.

Under high axial stretching, the typical head–tail structure is observed for low values of the strain-to-vorticity ratio, as shown in figure 11(*a*). However, for stronger strain flows, increased axial stretching enhances the leading dipole strength, causing it to travel faster than its tail, resulting in separation between the head and tail, as shown in figure 11(*b*). This is a key signature that can be observed during the reconnection of vortices (Hussain & Duraisamy 2011; Yao & Hussain 2020*b*), which can be used to identify the type of strain flow experienced by the vortices.

Quantitatively, we see that all strain-to-vorticity ratios considered are in the head–tail regime for high axial stretching, as shown in figure 12. Transition to the planar jet regime occurs at much higher $\mathcal{E}$. Pinch-off of the tail does not change the behaviour as the dipole still ejects vorticity into a new tail as the strain flow squeezes the leading dipole continuously.

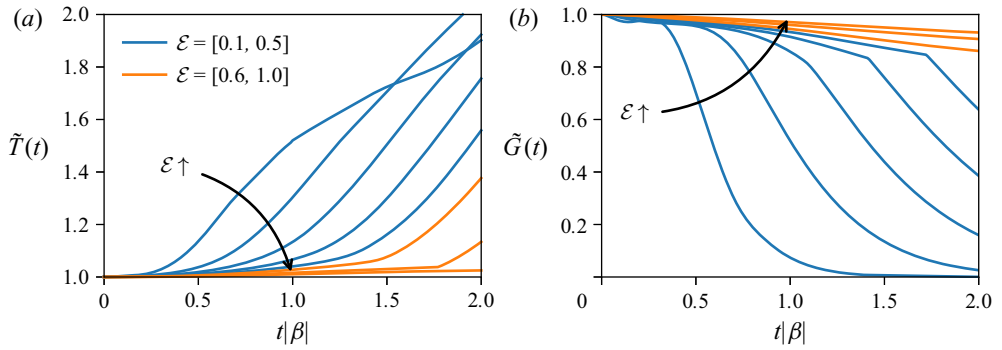

Figure 10. Time series of normalized (*a*) thickness $\tilde{T}(t)$ and (*b*) gap length $\tilde{G}(t)$ for the low axial stretching case. The head–tail regimes between $\mathcal{E} = 0.05, 0.1, 0.15, 0.2$ are shown in blue, while the plane jet regimes between $\mathcal{E} = 0.4, 0.6, 0.8, 1.0$ are shown in orange.

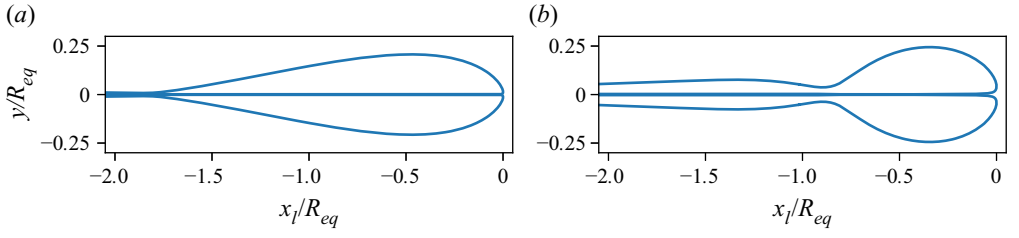

Figure 11. Contour snapshots of (*a*) $\mathcal{E} = 0.2$ and (*b*) $\mathcal{E} = 0.6$ at $t\,|\beta| = 2$ for the high axial stretching cases.

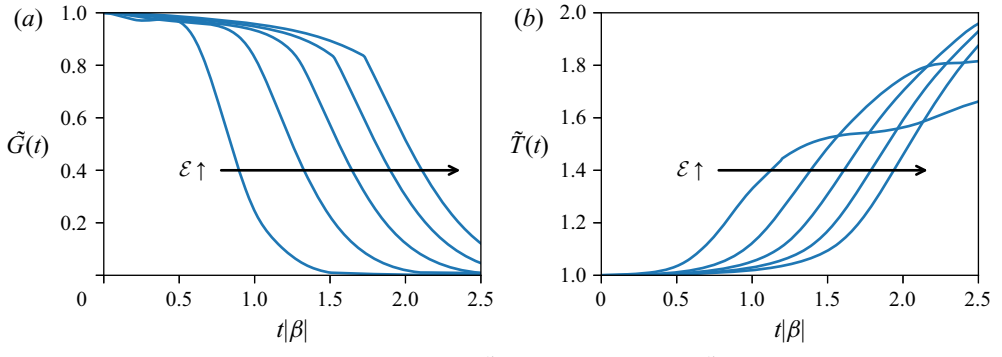

Figure 12. Time series of normalized (*a*) thickness $\tilde{T}(t)$ and (*b*) gap length $\tilde{G}(t)$ for the high axial stretching cases with $\mathcal{E} = 0.2$ to 1.0 at intervals of 0.2.

The limit of increasing axial strain flow is the axisymmetrical axial strain case. Under axisymmetrical axial strain, the dipole cores are finally able to maintain their compactness and remain as vortices, as shown by the contour snapshots in figure 13. The shape of the contour at $t\,|\beta| = 2$ is exactly the same as the initial condition but at a significantly reduced area due to vortex stretching. The centroid-to-equivalent radius also remains the same the entire time. That is, only high-strain flow is capable of maintaining the integrity of a vortex dipole.

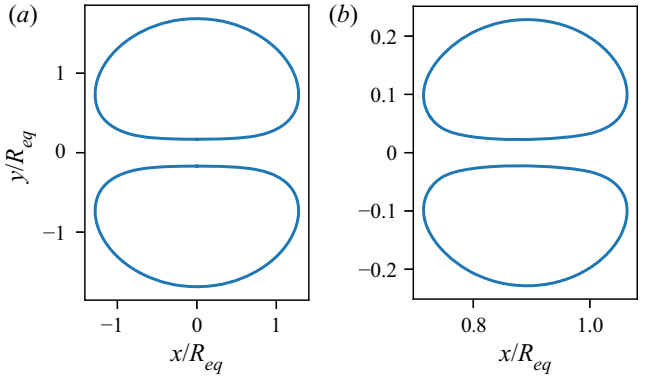

Figure 13. Contour snapshots of a vortex dipole in an axisymmetrical axial stretching strain flow with $\mathcal{E} = 1.0$ at (*a*) $t\,|\beta| = 0$ and (*b*) $t\,|\beta| = 2$.

5. Discussion

The implications of the reported strained dipole results to the ongoing discussions of the finite-time singularity and the turbulent cascade of anti-parallel vortex collision are discussed in this section.

5.1. *Finite-time singularity avoidance*

A significant criticism of the Biot–Savart 'tent' model by Moffatt & Kimura (2019*a*) is that direct numerical simulations of slender core anti-parallel vortex ring collision at $Re = 4000$ (Yao & Hussain 2020*b*) did not exhibit the predicted vorticity growth scaling. Yao & Hussain (2020*b*) speculated that two physical processes, namely, the braking effect of reconnection bridges and the head–tail separation, were omitted by Moffatt & Kimura (2019*a*), resulting in discrepancies between the theoretical modelling and numerical results. We have proposed previously that additional factors are at play to prevent Euler's equation finite-time singularity during anti-parallel vortex collisions (Hu & Peterson 2021). Specifically, we argued that at the time of the 'tent' apex curvature reversal, the reconnection bridges have yet to form due to the slower time scale of vortex reconnection relative to vortex motion, which implies that the braking effect plays a secondary role in halting the 'tent' development. As for the stripping of vorticity due to head–tail separation, our present results show that such a phenomenon occurs only when the vortex dipole overcomes the compressive strain flow from high axial stretching. That is, the loss of circulation from the tail separation is a transient effect and an indication that the effective strain-to-vorticity ratio is sufficiently high to prevent further core flattening. Numerical results of Yao & Hussain (2020*b*) and Hu & Peterson (2021) further support this claim as the colliding vortex cores at the apex maintain their compactness post tail separation.

We propose that the enhanced mutual induction from the asymmetrical deformation of vortex cores is the missing link between Moffatt & Kimura (2019*a*) and Yao & Hussain (2020*b*). As reported in Hu & Peterson (2021), we observed in prior direct numerical simulations that curvature reversal occurs when the colliding vortex tubes break the 'tent' form, which we referred to as 'parallelization'. We speculate that the enhanced mutual induction observed in the present work drives parallelization between colliding vortices as illustrated in figure 14. The compact vortex core assumption (associated with the monopole model) is one of the fundamental requirements for the 'tent' model; hence

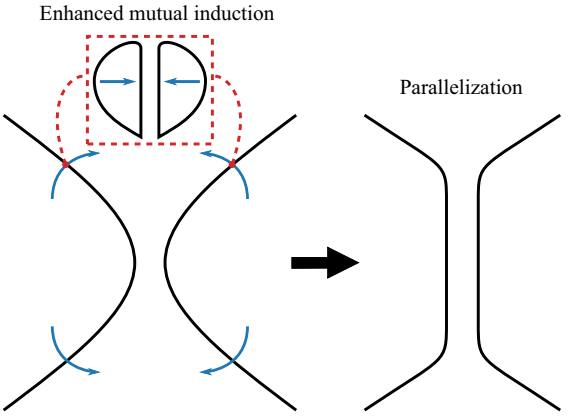

Figure 14. Schematic of the parallelization process, introduced in Hu & Peterson (2021), during anti-parallel vortex reconnection and the role of enhanced mutual attraction. The top view of the 'tent' process is shown, and black lines represent the colliding vortices.

the model is, by definition, unable to predict arresting of the 'tent' formation process and the subsequent avoidance of a finite-time singularity, driven by asymmetrical core deformation as observed herein. However, the universality of the proposed enhanced mutual induction-driven parallelization process remains unknown. Careful analysis of the scaling between the curvature-induced strain, which also becomes stronger as the curvature develops at the apex of the 'tent', and vortex stretching during the formation of the 'tent', remains to be examined.

Finally, we would like to point out that a major assumption employed by Moffatt & Kimura (2019*a*) and the present contour dynamics simulations is two-dimensionality, which neglects stretching and axial flow that can arise in a three-dimensional non-uniform strain field. These effects would undoubtedly play a major role during the collision of anti-parallel vortices. However, the goal of the present study is to highlight the consequences of dipole core deformation using a two-dimensional approximation to gain some insights into the complex problem of anti-parallel vortex interaction.

5.2. *Turbulent cascade*

Recent surveys have shown that turbulent flows are composed of a self-similar hierarchy of anti-parallel pairs of vortex tubes (Goto *et al.* 2017; Motoori & Goto 2019), for which the vortex dipole model can be considered a fundamental element. There are competing frameworks explaining the turbulent cascade in terms of the interaction of anti-parallel vortices. Brenner *et al.* (2016) introduced a turbulent cascade model wherein vortices iteratively flatten into vortex sheets and then re-roll into smaller vortices. Experiments by McKeown *et al.* (2018) support this, in which up to three iterations of the flattening and re-spiralling process were observed. In contrast, a numerical study of a pair of straight vortex tubes by McKeown *et al.* (2020) did not observe the iterative flattening process. Rather, an iterative process of elliptical instabilities was discovered. The contact between vortex tubes at large amplitudes triggered the vortex reconnection, which Yao & Hussain (2020*a*) proposed to be an alternative framework of turbulent cascade via anti-parallel vortex interaction (interested readers are also pointed to the excellent review article by Yao & Hussain 2021).

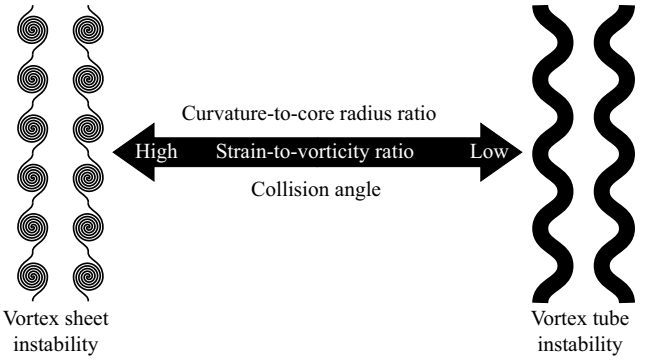

Figure 15. Spectrum of instabilities during an anti-parallel vortex collision.

Given the complexity of turbulence, it is unlikely that a single mechanism is responsible for the entirety of the energy cascade. Our findings have shown that an interacting vortex pair can turn into a head–tail structure or flatten into vortex sheets, depending on the strain-to-vorticity ratio. Herein we found flattening to occur in high strain-to-vorticity ratio scenarios, such as a high curvature-to-core radius ratio (Kida *et al.* 1991*b*) and/or a high collision angle (McKeown *et al.* 2018; Hu & Peterson 2021). In such conditions, it is tenable that vortex sheet instabilities would drive the iterative cascade process, as suggested by Brenner *et al.* (2016). Conversely, we observed a head–tail structure formation in low strain-to-vorticity ratio scenarios, where the leading vortex dipole is the dominant feature. In these scenarios, vortex tube instabilities (McKeown *et al.* 2020) and the subsequent vortex reconnections would likely be the primary mechanism responsible for the turbulent cascade. That is, the present work offers a framework wherein seemingly disparate turbulent cascade mechanisms can be unified through the strain-to-vorticity ratio as illustrated in figure 15.

6. Conclusion

In this study, we surveyed the evolution of a vortex dipole in an external strain flow, which behaves qualitatively and quantitatively differently from the well-studied vortex monopole. Under an imposed strain flow, vortex dipoles do not maintain their compactness as a result of each vortex patch preventing the self-induced rotation of the other. Hence the deformation is always aligned with the strain flow, resulting in the dipole compressing indefinitely. This has implications for the search for a finite-time singularity of Euler's equation through anti-parallel vortex collision and proposed turbulent cascade mechanisms. Regarding the former, our results suggest that the validity of the Euler's equation finite-time singularity model of Moffatt & Kimura (2019*a*) appears to depend on the ratio between the strength of the curvature-induced strain flow and the vorticity density of the dipole cores en route to the potential singularity. If the ratio reaches an asymptotic value that is strongly biased towards the vorticity density, then a finite-time singularity may be possible due to the disparity between the flattening and convective time scales. If curvature-induced strain flow dominates, then vortex sheets will form instead. Regarding the turbulent cascade, we show that, depending on the strain-to-vorticity ratio, strained dipole evolution can result in the formation of vortex sheets or a well-defined head–tail structure. These two configurations, vortex sheets and vortex tubes, serve as fundamental elements of competing turbulent cascade models. Our work demonstrates

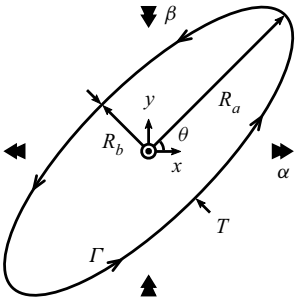

Figure 16. Schematic of a vortex monopole in an irrotational strain flow.

a physical mechanism whereby these two foundational configurations can both arise naturally, suggesting that both cascade mechanisms may play a role in turbulence.

Funding. This research received no specific grant from any funding agency, commercial or not-for-profit sectors.

Declaration of interests. The authors report no conflict of interest.

Author ORCIDs.
Sean D. Peterson https://orcid.org/0000-0001-8746-2491.

Appendix A. Vortex monopole

In this appendix, we present the results for an initially circular vortex monopole in the same external strain flow in table 1 to provide a baseline for the dipole study. In particular, the principal axes length ratio (R_a/R_b, see figure 16) is the primary quantitative results reported in the literature (Kida 1981; Neu 1984), which does not apply to the dipole study. Instead, we employ the thickness parameter $T = 2\min(R_a, R_b)$ as the measurement of the compactness of the vortex core to facilitate comparisons with the dipole results.

The vortex monopole remains elliptical at all times in the strain flow, and its motion is governed by the following set of ordinary differential equations:

$$\frac{\mathrm{d}R_a}{\mathrm{d}t} = R_a(\alpha\cos^2\theta + \beta\sin^2\theta), \tag{A1a}$$

$$\frac{\mathrm{d}R_b}{\mathrm{d}t} = R_b(\beta\cos^2\theta + \alpha\sin^2\theta), \tag{A1b}$$

$$\frac{\mathrm{d}\theta}{\mathrm{d}t} = \Omega(t)\,\frac{R_aR_b}{(R_a+R_b)^2} - \frac{\alpha-\beta}{2}\,\frac{R_a^2+R_b^2}{R_a^2-R_b^2}\sin 2\theta, \tag{A1c}$$

where θ is the orientation of the vortex monopole (Neu 1984). The results reported here are obtained with (A1), though it was confirmed that the contour dynamics method described in § 2 yielded identical results (see Appendix B for a comparison sample).

The equations of motion for the monopole can be decomposed into two major effects. The first is the self-rotation of an elliptical vortex captured by the first term in (A1*c*), which states that a higher ellipticity of the vortex monopole corresponds to a lower self-rotation rate. Second, the irrotational strain field can be decomposed into a linear (symmetric) and a rotational (anti-symmetric) component, depending on the bearing (θ) of the principal axes. As the monopole reorients under its self-induced rotation, the linear component of

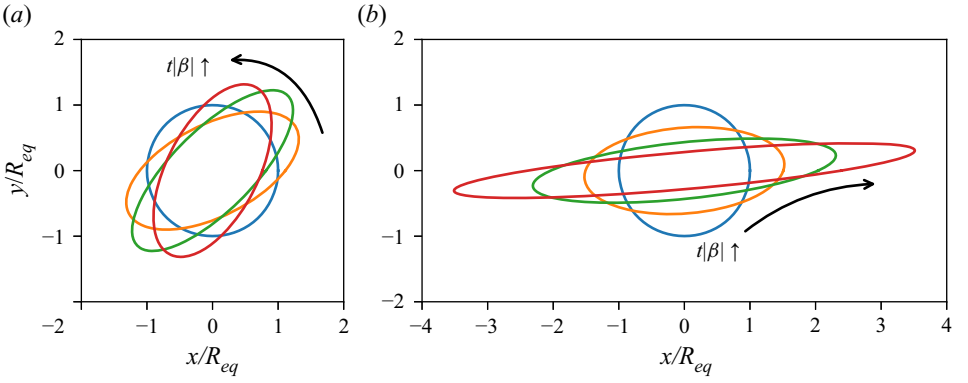

Figure 17. Snapshots of a vortex monopole in a planar strain flow with strain-to-vorticity ratio (*a*) $\mathcal{E} = 0.1$ and (*b*) $\mathcal{E} = 0.6$, at a time interval $t\,|\beta| = 0.426$.

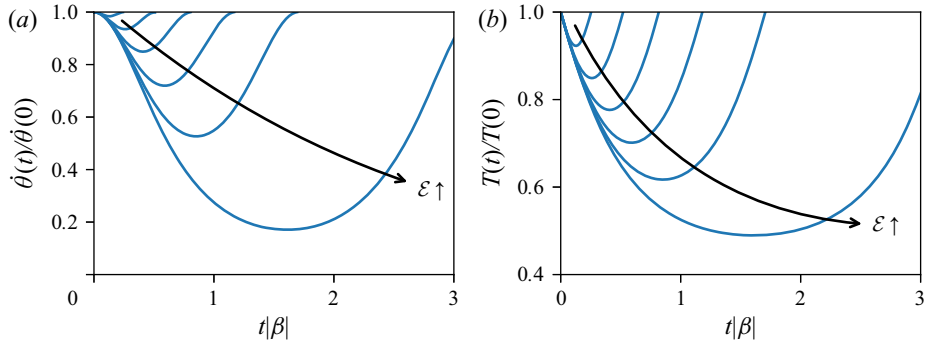

Figure 18. Evolution of (*a*) the rotation rate $\dot{\theta}(t)$, and (*b*) the thickness $T(t)$, of a vortex monopole in a planar strain field with strain-to-vorticity ratio $\mathcal{E} = 0.02$ to 0.12 at intervals of 0.02. One period of oscillation is shown for clarity.

the strain flow can either flatten or compact the vortex core, which in turn influences the rotation rate.

For the planar strain listed in table 1, the vortex motion bifurcates into either averaging or flattening regimes, as shown in figure 17. For the averaging regime in figure 17(*a*), the strain flow elongates the monopole into an ellipse. Once the major axis passes $\theta = 45^\circ$, where the maximum aspect ratio occurs, the strain flow compresses the boundary back to a circular shape. For the flattening regime in figure 17(*b*), the major axis never rotates past $\theta = 45^\circ$ because the anti-clockwise self-rotation halts and the strain flow flattens the monopole indefinitely into a sheet.

Quantitative results for the averaging regime for planar strain flow are shown in figure 18. Prior to the major axis reaching $\theta = 45^\circ$, the rotation rate $\dot{\theta}$ decelerates under the influence of both the counter-rotating strain component and increased monopole ellipticity, as shown in figure 18(*a*). Therefore, a stronger strain field results in a slower rotation rate, which corresponds to a longer period of thickness oscillation in figure 18(*b*). However, the deceleration is insufficient to prevent the monopole from moving past $\theta = 45^\circ$, after which the strain flow compacts the vortex back to the circular shape; hence oscillation of the vortex increases, but it never flattens.

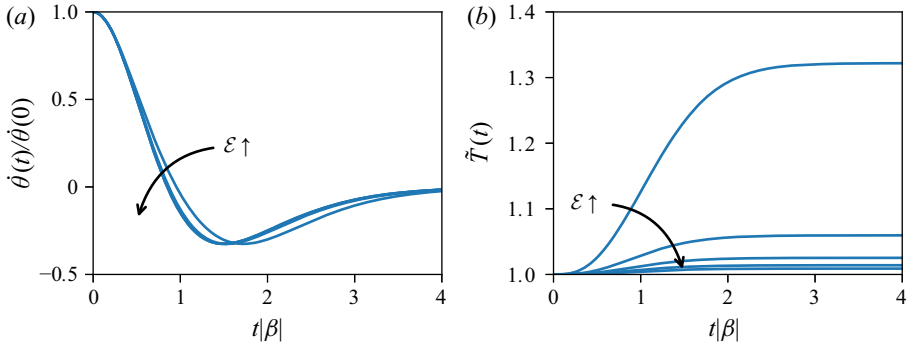

Figure 19. Evolution of (*a*) the rotation rate $\dot{\theta}(t)$, and (*b*) the normalized thickness $\tilde{T}(t)$, for a vortex monopole in a planar strain field with strain-to-vorticity ratio $\mathcal{E} = 0.2$ to 1.0 at intervals of 0.2.

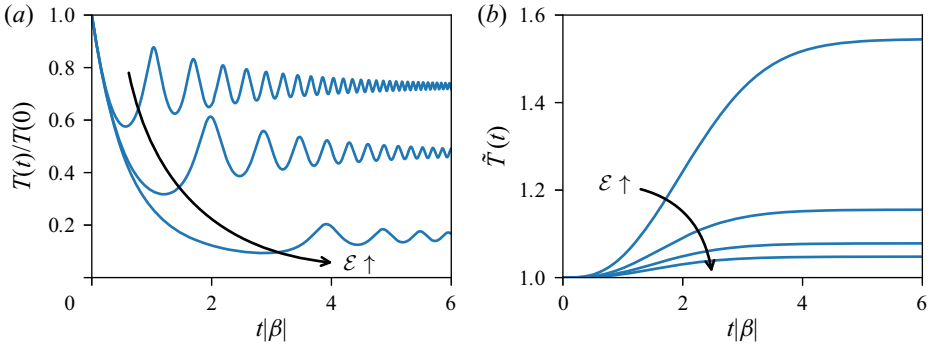

Figure 20. Evolution of (*a*) the thickness $T(t)$, and (*b*) the normalized thickness $\mathcal{T}(t)$, for a vortex monopole in a low axial strain flow with (*a*) $\mathcal{E} = 0.1$ to 0.3 at intervals of 0.1, and (*b*) $\mathcal{E} = 0.4$ to 1.0 at intervals of 0.2.

For $\mathcal{E} \geq 0.123$, the strain flow prevents the major axis of the elliptical vortex monopole from passing $\theta = 45^\circ$, and reverses the monopole self-rotation as shown in figure 19(*a*). As such, the principal axes of the vortex are oriented with the flattening strain field, which compresses the monopole into a vortex sheet. A transient period can be seen from the normalized thickness evolution in figure 19(*b*) because of the initial misalignment, but as time progresses, the counter-rotating component of the strain flow re-aligns the principal axes between the strain flow and the vortex. Thus the vortex flattens at the same rate as a simple material surface, as shown by the levelled normalized thickness at large times in figure 19(*b*). Note that the normalized thickness is defined as $\mathcal{T}_1 = T_1(t)/\exp(\beta t)$, which highlights the role of vorticity on the thickness evolution in contrast to a vorticity-free material contour under the same compression.

Introducing weak axial stretching pushes the bifurcation limit to $\mathcal{E} \geq 0.317$. Stretching effectively lowers the strain-to-vorticity ratio $\mathcal{E}$ dynamically, hence we see a gradual decrease in the magnitude of the thickness oscillation for the averaging regime in figure 20(*a*). For the flattening regime in figure 20(*b*), the added weak axial stretching extends the transition period, but the strain flow still re-aligns with the principal axes of the vortex monopole in the end, then flattens the vortex like a simple material surface at large times. Further strengthening of the axial stretching only exaggerates this effect.

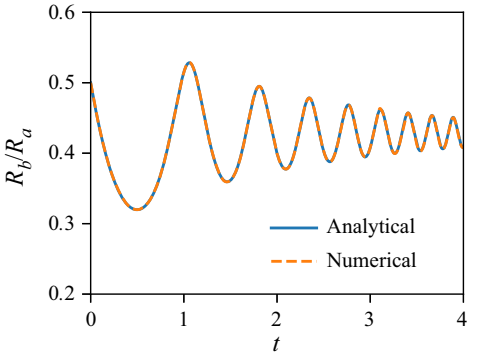

Figure 21. Aspect ratio R_b/R_a comparison between the analytical and numerical results for a vortex monopole in a low axial strain field with $\mathcal{E} = 0.1$.

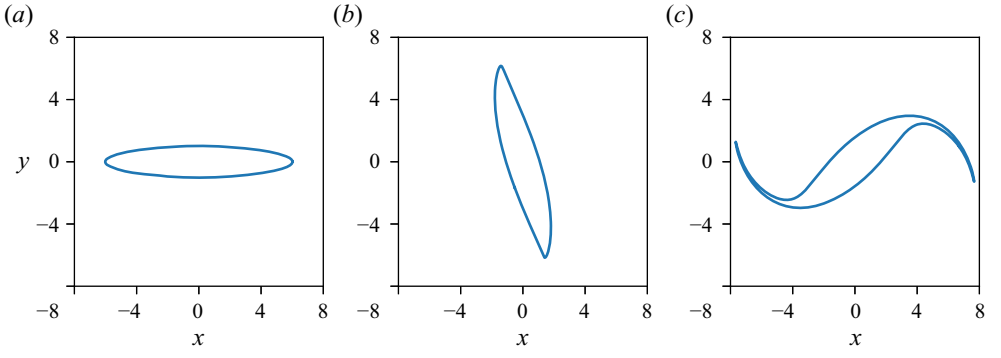

Figure 22. Evolution of a Kirchhoff elliptical vortex with aspect ratio 6 : 1 and $m = 4$ perturbation. Snapshots from (*a*) $t = 0$, (*b*) $t = 15$ and (*c*) $t = 30$ are shown.

Appendix B. Validation

Here, we compare our numerical contour dynamics results with three classical problems in the literature in order to validate our numerical method. We first compare our strained monopole numerical results with the analytical solutions from (A1) to check the accuracy of axial stretching implementation. A sample comparison with initial conditions $R_b/R_a = 0.5$ and $\theta = 0^\circ$ in a low axial strain field (see table 1) with $\mathcal{E} = 0.1$ is shown in figure 21. The time series of the aspect ratio is identical between the analytical results and our numerical results.

Next, we simulate the evolution of a perturbed Kirchhoff elliptical vortex (Dritschel 1986; Mitchell & Rossi 2008). In particular, a Kirchhoff vortex under an $m = 4$ perturbation generates a tail-like feature that somewhat resembles a dipole tail, which provides a reasonable test case for our solution methodology. Numerical results of a Kirchhoff vortex with aspect ratio 6 : 1, vorticity density $\Omega = 1$, and $m = 4$ perturbation magnitude 0.02 are shown in figure 22, which captures the double spiralling tails as expected.

Finally, we simulate the coalescence of two same-signed vortices to check if our numerical scheme can capture the interaction between two separated vortex patches in close proximity. Figure 23 illustrates the results of two equal vortices with radii $R = 1$ and vorticity density $\Omega = 1$ separated by $3.5R$ between their centres. Our solution exhibits

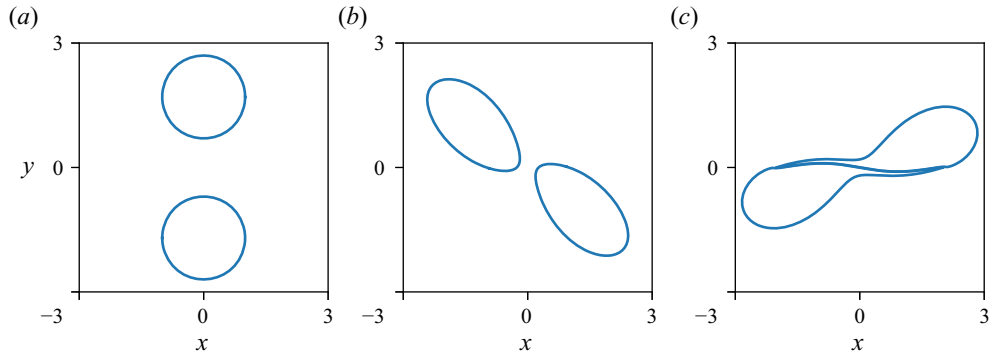

Figure 23. Coalescence of same-signed circular vortices with radius $R = 1$ and separated by $3.5R$. Snapshots from (*a*) $t = 0$, (*b*) $t = 10$ and (*c*) $t = 20$ are shown.

the documented behaviour in the literature wherein the circular vortices are deformed into comma-like shapes as they merge (see figure 23*c*).

References

Brenner, M.P., Hormoz, S. & Pumir, A. 2016 Potential singularity mechanism for the Euler equations. *Phys. Rev. Fluids* **1**, 084503.

Buntine, J.D. & Pullin, D.I. 1989 Merger and cancellation of strained vortices. *J. Fluid Mech.* **205**, 263–295.

Delbende, I. & Rossi, M. 2009 The dynamics of a viscous vortex dipole. *Phys. Fluids* **21**, 073605.

Dritschel, D.G. 1986 The nonlinear evolution of rotating configurations of uniform vorticity. *J. Fluid Mech.* **172**, 157–182.

Goto, S., Saito, Y. & Kawahara, G. 2017 Hierarchy of antiparallel vortex tubes in spatially periodic turbulence at high Reynolds numbers. *Phys. Rev. Fluids* **2**, 064603.

Hu, J. & Peterson, S.D. 2021 The influence of collision angle for viscous vortex reconnection. *Phys. Fluids* **33**, 093608.

Hussain, F. & Duraisamy, K. 2011 Mechanics of viscous vortex reconnection. *Phys. Fluids* **23**, 021701.

Jacobs, P.A. & Pullin, D.I. 1985 Coalescence of stretching vortices. *Phys. Fluids* **28** (6), 1619–1625.

Kida, S. 1981 Motion of an elliptic vortex in a uniform shear flow. *J. Phys. Soc. Japan* **50** (10), 3517–3520.

Kida, S. & Takaoka, M. 1994 Vortex reconnection. *Annu. Rev. Fluid Mech.* **26**, 169–189.

Kida, S., Takaoka, M. & Hussain, F. 1991*a* Collision of two vortex rings. *J. Fluid Mech.* **230**, 583–646.

Kida, S., Takaoka, M. & Hussain, F. 1991*b* Formation of head–tail structure in a two-dimensional uniform straining flow. *Phys. Fluids* A **3** (11), 2688–2697.

McKeown, R., Ostilla-Mónico, R., Pumir, A., Brenner, M.P. & Rubinstein, S.M. 2018 Cascade leading to the emergence of small structures in vortex ring collisions. *Phys. Rev. Fluids* **3**, 124702.

McKeown, R., Ostilla-Mónico, R., Pumir, A., Brenner, M.P. & Rubinstein, S.M. 2020 Turbulence generation through an iterative cascade of the elliptical instability. *Sci. Adv.* **6** (9), eaaz2717.

Meleshko, V.V. & van Heijst, G.J.F. 1994 On Chaplygin's investigations of two-dimensional vortex structures in an inviscid fluid. *J. Fluid Mech.* **272**, 157–182.

Mitchell, T.B. & Rossi, L.F. 2008 The evolution of Kirchhoff elliptic vortices. *Phys. Fluids* **20** (5), 054103.

Moffatt, H.K., Kida, S. & Ohkitani, K. 1994 Stretched vortices – the sinews of turbulence; large-Reynolds-number asymptotics. *J. Fluid Mech.* **259**, 241–264.

Moffatt, H.K. & Kimura, Y. 2019*a* Towards a finite-time singularity of the Navier–Stokes equations. Part 1. Derivation and analysis of dynamical system. *J. Fluid Mech.* **861**, 930–967.

Moffatt, H.K. & Kimura, Y. 2019*b* Towards a finite-time singularity of the Navier–Stokes equations. Part 2. Vortex reconnection and singularity evasion. *J. Fluid Mech.* **870**, R1.

Moore, D.W. & Saffman, P.G. 1971 Structure of a line vortex in an imposed strain. In *Aircraft Wake Turbulence and Its Detection* (ed. J.H. Olsen, A. Goldburg & M. Rogers), pp. 339–354. Springer.

Motoori, Y. & Goto, S. 2019 Generation mechanism of a hierarchy of vortices in a turbulent boundary layer. *J. Fluid Mech.* **865**, 1085–1109.

Neu, J.C. 1984 The dynamics of a columnar vortex in an imposed strain. *Phys. Fluids* **27** (10), 2397–2402.

PIERREHUMBERT, R.T. 1980 A family of steady, translating vortex pairs with distributed vorticity. *J. Fluid Mech.* **99**, 129–144.

PUMIR, A. & SIGGIA, E.D. 1990 Collapsing solutions to the 3-D Euler equations. *Phys. Fluids* A **2**, 220–241.

SAFFMAN, P.G. & TANVEER, S. 1982 The touching pair of equal and opposite uniform vortices. *Phys. Fluids* **25**, 1929–1930.

SIGGIA, E.D. & PUMIR, A. 1985 Incipient singularities in the Navier–Stokes equations. *Phys. Rev. Lett.* **55**, 1749–1752.

TRIELING, R.R., VAN WESENBEECK, J.M.A. & VAN HEIJST, G.J.F. 1998 Dipolar vortices in a strain flow. *Phys. Fluids* **10**, 144–159.

YAO, J. & HUSSAIN, F. 2020*a* A physical model of turbulence cascade via vortex reconnection sequence and avalanche. *J. Fluid Mech.* **883**, A51.

YAO, J. & HUSSAIN, F. 2020*b* On singularity formation via viscous vortex reconnection. *J. Fluid Mech.* **888**, R2.

YAO, J. & HUSSAIN, F. 2021 Vortex reconnection and turbulence cascade. *Annu. Rev. Fluid Mech.* **54**, 317–347.

ZABUSKY, N.J., HUGHES, M.H. & ROBERTS, K.V. 1979 Contour dynamics for the Euler equations in two dimensions. *J. Comput. Phys.* **30**, 96–106.